Electronic Supplementary Information

Electrostatic Gating of Single-Molecule Junctions Based on the STM-BJ technique

Ping Zhou,[a] Jueting Zheng,[a] Tianyang Han,[a] Lijue Chen,[a] Wenqiang Cao,[a] Yixuan Zhu,[a] Dahai Zhou,[a] Ruihao Li,[a] Yingyu Tian,[a] Zitong Liu,[b] Junyang Liu*[,a] and Wenjing Hong*[,a]

Affiliations:

a. State Key Laboratory of Physical Chemistry of Solid Surfaces, College of Chemistry and Chemical Engineering, *i*ChEM, Xiamen University, Xiamen, 361005, China.

b. State Key Laboratory of Applied Organic Chemistry (SKLAOC), College of Chemistry and Chemical Engineering, Lanzhou University, Lanzhou 730000, P. R. China

*Email of corresponding authors:

whong@xmu.edu.cn.

jyliu@xmu.edu.cn.

Table of Contents

S1. The target compounds in this work.

The structure of molecules, as shown in Figure S1. The molecules anchored by –Py and –CN were used in this paper were purchased from Shanghai Tensus Biotech CO., Ltd. The purity of these samples was 99.5%. The $–SCH_3$ anchored tribiphenyl was synthesized using the previously reported protocol.[1] The 1,2,4-trichlorobenzene (TCB, 99%) was bought from Aladdin. The Tetrakis(dimethyl amido)hafnium (TDMAHf) for deposition of dielectric layers was bought from STREM Chemicals.

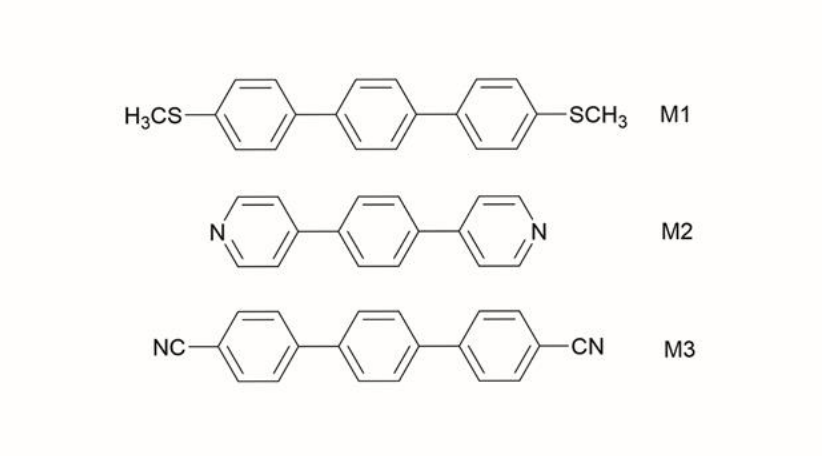

Figure S1. The structure of **M1**, **M2**, **M3**, respectively.

S2. Experimental technique

Preparation of STM tips

A gold wire of 0.25 mm diameter (99.99%, Jiaming, Beijing) was clean and annealed by butane flame into a golden bead to form the gold-gold atomic contact at the sharpest location.

Preparation of the substrates

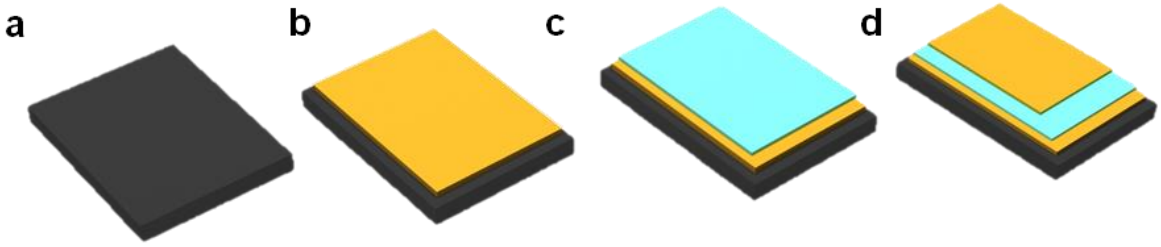

Figure S2. Fabrication process of gate-tunable substrate. (a) the pre-cleaned silicon wafer. (b) the deposition of gate electrode. (c) ALD for HfO_2 growth (d) fabrication for substrate using a metal mask.

The fabrication process of the gate-tunable substrate is schematically illustrated in Figure S2. The first step is cleaning pretreatment. The silicon wafer was pre-cleaned by piranha solution that the ratio of concentrated sulfuric acid to hydrogen peroxide is 3:1 to remove organic residues from the surface of silicon wafer, then the 33% hydrofluoric acid solution was used to remove the oxide layer. The purpose of the those is to achieve smaller surface roughness of silicon wafer to ensure that we can deposit a high-quality HfO_2 in a subsequent process to avoid the edge effect of thin-film growth. 20/200 nm Cr/Au is deposited above the 500 μm silicon wafer by magnetron sputtering as the back-gate electrode, as shown in Figure S2 (b). This procedure should be done immediately to keep the silicon substrates out of oxidation in the air. In the third step, as shown in Figure S2 (c), a commercial Beneq TFS 200 Atomic Layer Deposition (ALD) system was used to deposit HfO_2 layer on the top 200 nm thick Au film. Tetrakis(dimethyl amido)hafnium (TDMAHf) bought from Suzhou Fenna Electronic Technology Co. LTD., and ultrapure water were used as the hafnium and oxygen source, respectively. Nitrogen gas with a purity of 99.99% was used as the carrier and purge gas. According to previous literature, we deposited 25 nm HfO_2 at 200±3℃ of the ALD reaction chamber.[2, 3] The thickness of HfO_2 and deposition temperature is essential for obtaining a high-quality insulating layer, significantly

determining the gating efficiency. The ALD process parameters as follows: number of the cycle: 250, TDMAHf pulse time: 500 ms; TDMAHf purge time: 3000 ms; H_2O pulse time: 100 ms; H_2O purge time: 1500 ms; N_2 carrier and purge gas flow: 200 sccm. Finally, we designed a metal mask for depositing 100 nm Au without an adhesion layer as the source electrode by electron beam evaporation of after plasma activation, as shown in Figure S2 (d).

The leakage current of hafnium oxide

We randomly picked three chips and measured the leakage current of the hafnium oxide layer when V_g was swept from -12 V to 12 V. The result shows that the leakage current is at pA-level for all chips under the gate voltage at least 11 V, only one of them was damaged when the voltage increased to above 11 V, as shown in Figure S3. Since the conductance of molecules is at nA-level in our works (the molecular conductances in our study mainly locate around 10^{-5} G_0 to 10^{-3} G_0), and the source/drain voltage is 0.1 V), the leakage current does not affect the conductance measurement and the insulating layer has good compactness, and the yield of the sample is relatively high.

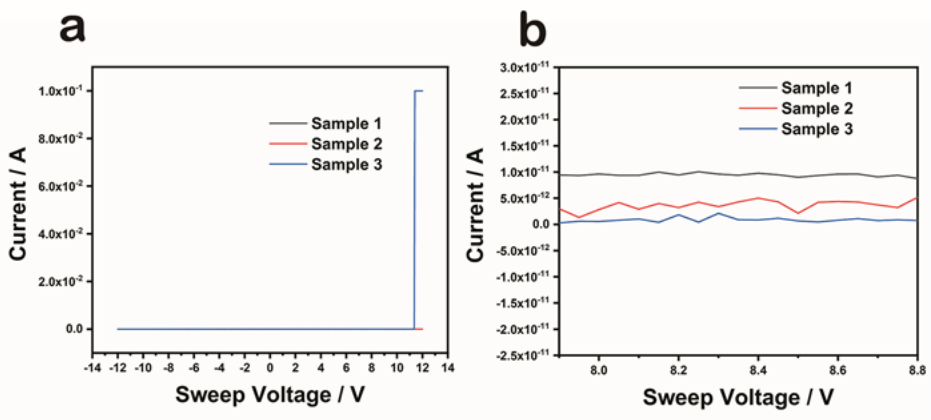

Figure S3. (a) The leakage current of the hafnium oxide when V_g was swept from -12 V to 12 V. (b) Partial enlargement of (a).

Measurement of single-molecule conductance and the conductance versus V_g

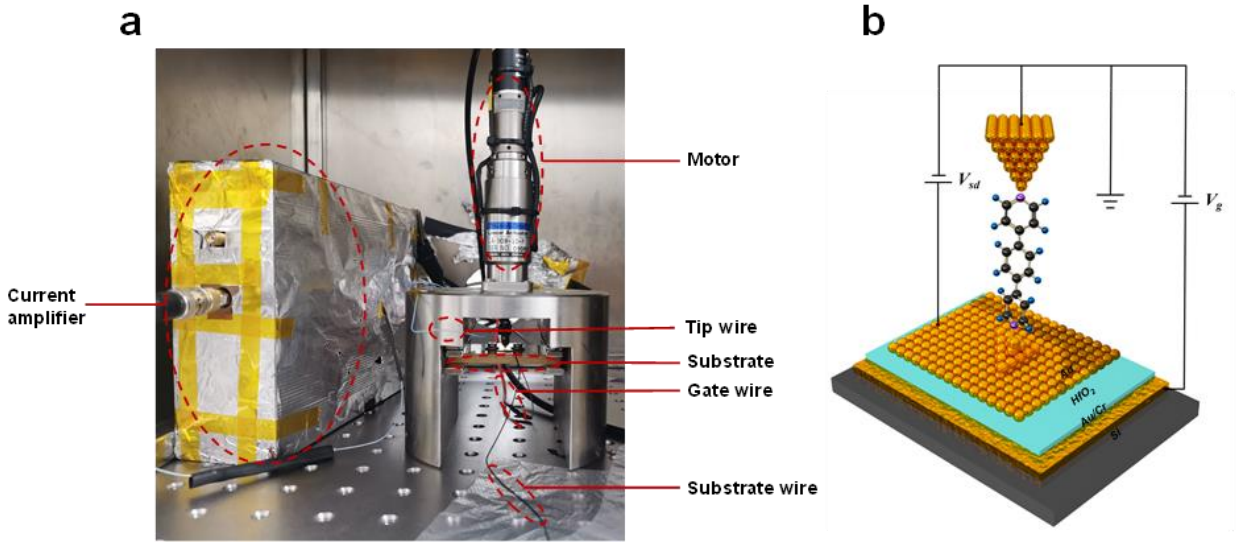

Figure S4. Experimental instrument of home-built STM-BJ. (a) Important parts of STM-BJ instrument. (b) the diagram of circuit connection.

Single-molecule conductance measurements were obtained at room temperature using the scanning tunneling microscope break junction technique (STM-BJ) shown in Figure S3. To avoid breaking the HfO_2 layer, we set an upper limit of current during electrical signal acquisition. We also test the insulation of the HfO_2 layer before and after the experiment by connecting the substrate to the gate electrode, as shown in Figure S5, the current is at the pA-level (blue line). During STM-BJ measurement, just like a standard test reported by many articles,[4-6] a 100 mV DC bias voltage was applied between the gold substrate and the tip. A stepping motor and a piezoelectric actuator were used as the driving tools to control the distance between the STM gold tip and substrate at the nanoscale. A lab-built logarithmic I-V converter collected the tunneling current with a sampling rate of 20 kHz. The only difference from the standard test is that we would apply different V_g in the gate electrode by

introducing the gate wire port shown in Figure S4.

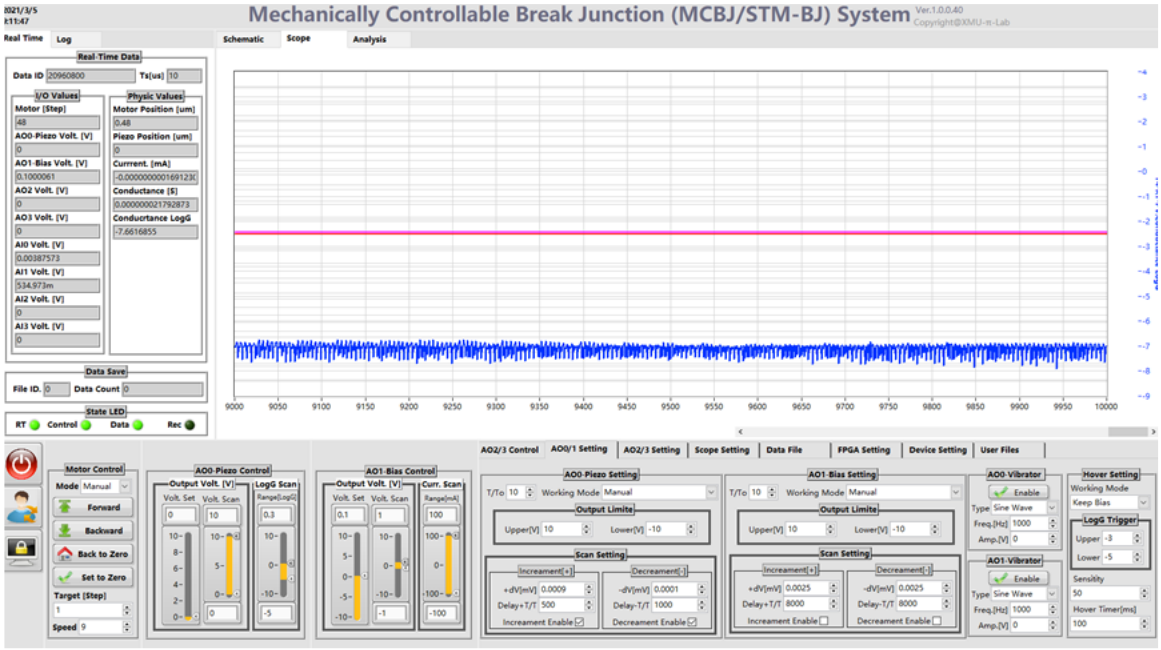

Figure S5. The leakage current measurement after connecting the substrate and gate electrode. (The blue line represents the leakage current between source electrode and gate electrode.)

S3. Additional data

The conductance-distance traces were collected and analyzed for each molecule to form the 1D histograms and 2D conductance-displacement histograms that reflect the molecular conductance and length, the 1D histograms and 2D conductance-displacement histograms and the number of single curves are as follows.

1D histograms for M1 at different V_g

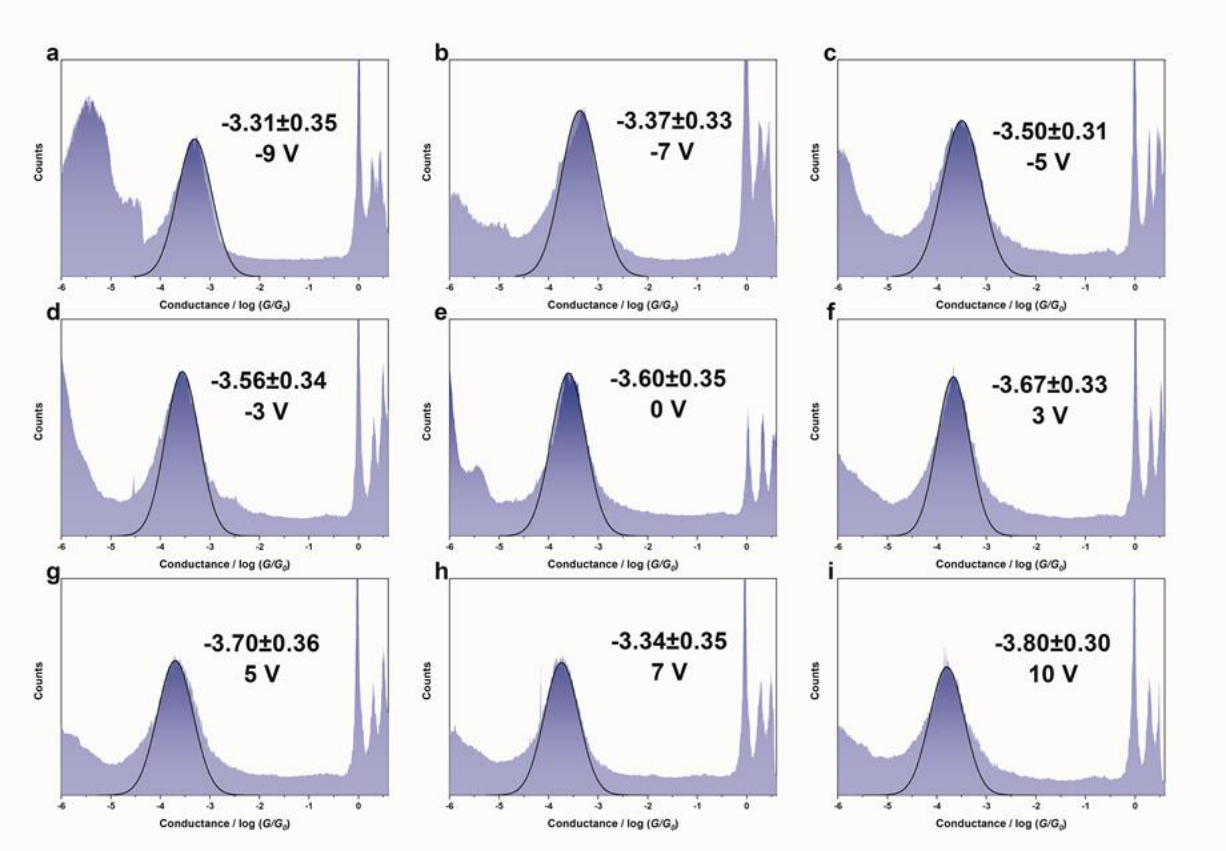

Figure S6. The results of 1D histograms for **M1** at different V_g. (a) -9 V; (b) -7 V; (c) -5 V; (d) -3 V; (e) 0 V; (f) 3 V; (g) 5 V; (h) 7 V; (i) 10 V.

2D conductance-displacement histograms for M1 at different V_g

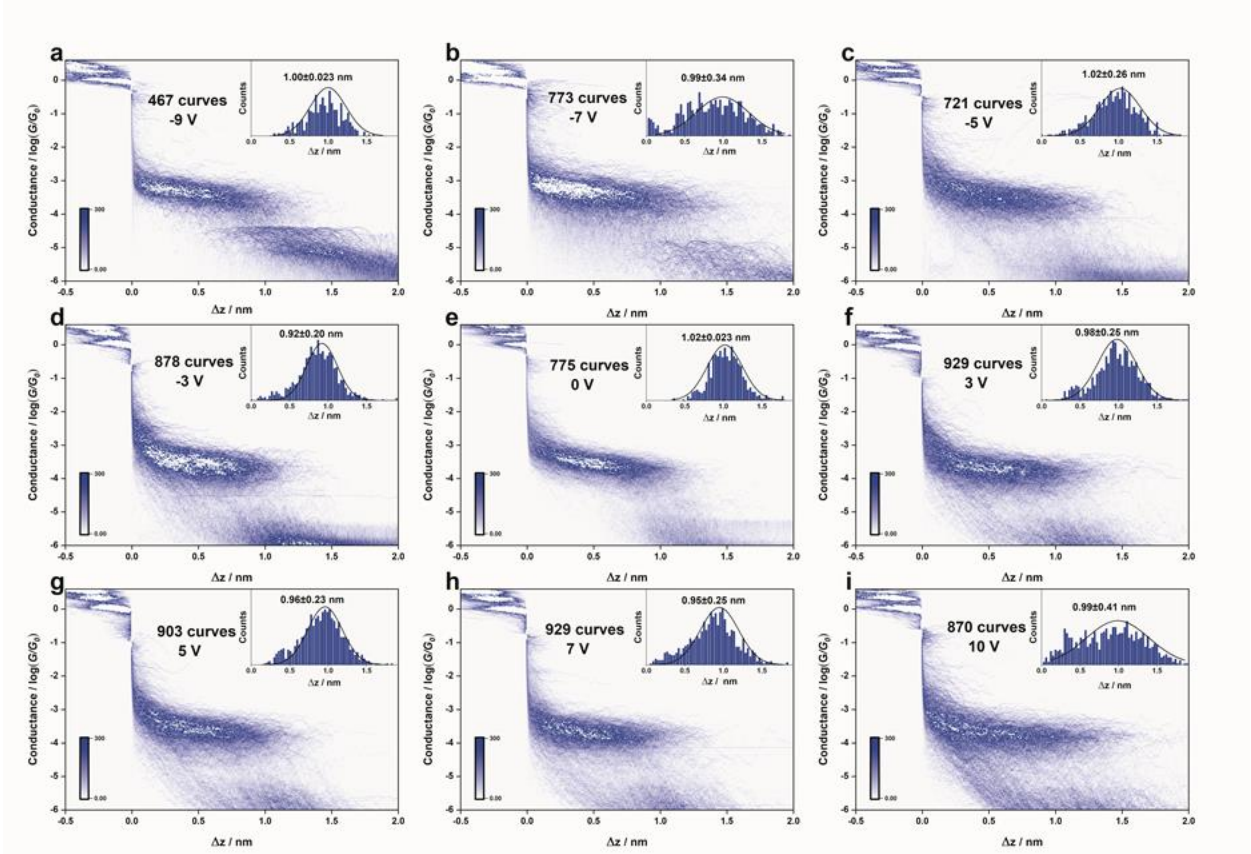

Figure S7. The results of 2D conductance-displacement histograms for **M1** at different V_g. (a) -9 V; (b) -7 V; (c) -5 V; (d) -3 V; (e) 0 V; (f) 3 V; (g) 5 V; (h) 7 V; (i) 10 V.

1D histograms for M2 at different V_g

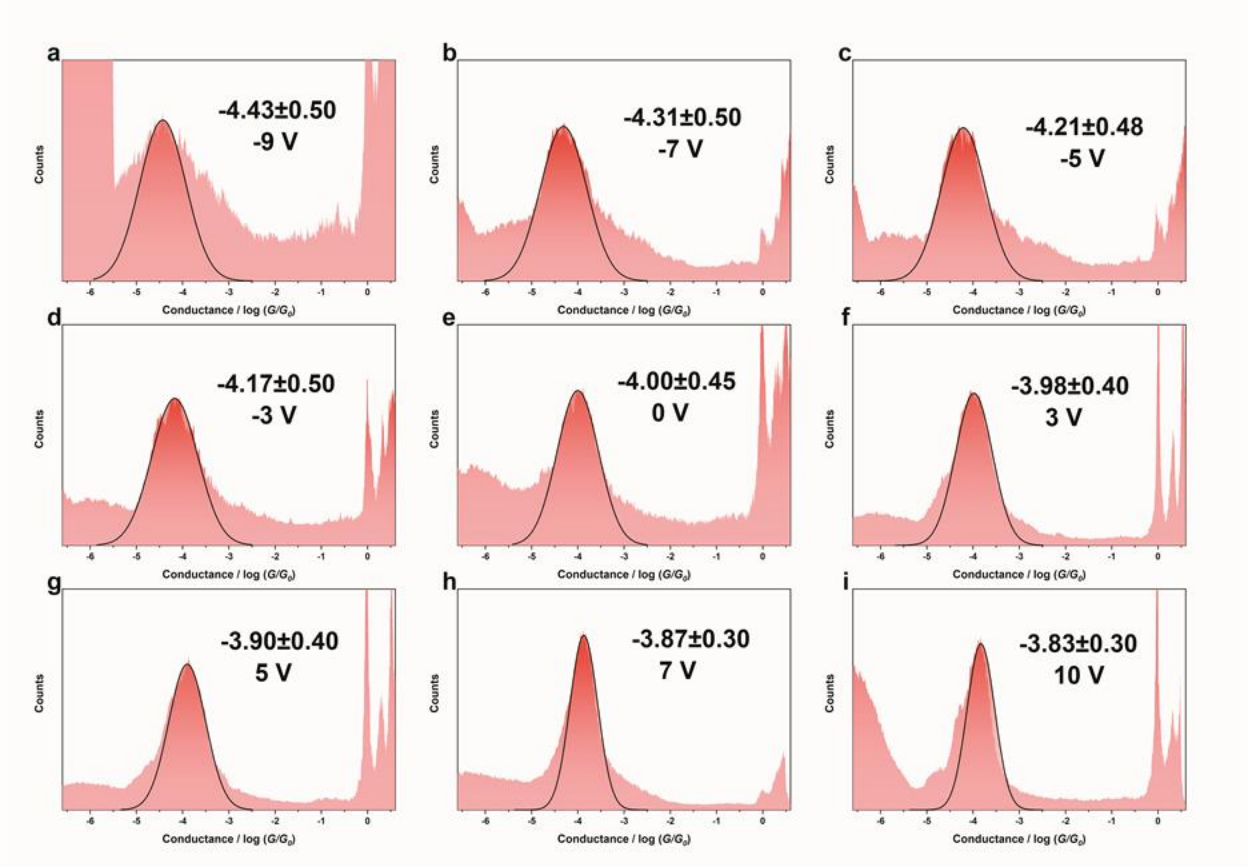

Figure S8. The results of 1D histograms for **M2** at different V_g. (a) -9 V; (b) -7 V; (c) -5 V; (d) -3 V; (e) 0 V; (f) 3 V; (g) 5 V; (h) 7 V; (i) 10 V.

2D conductance-displacement histograms for M2 at different V_g

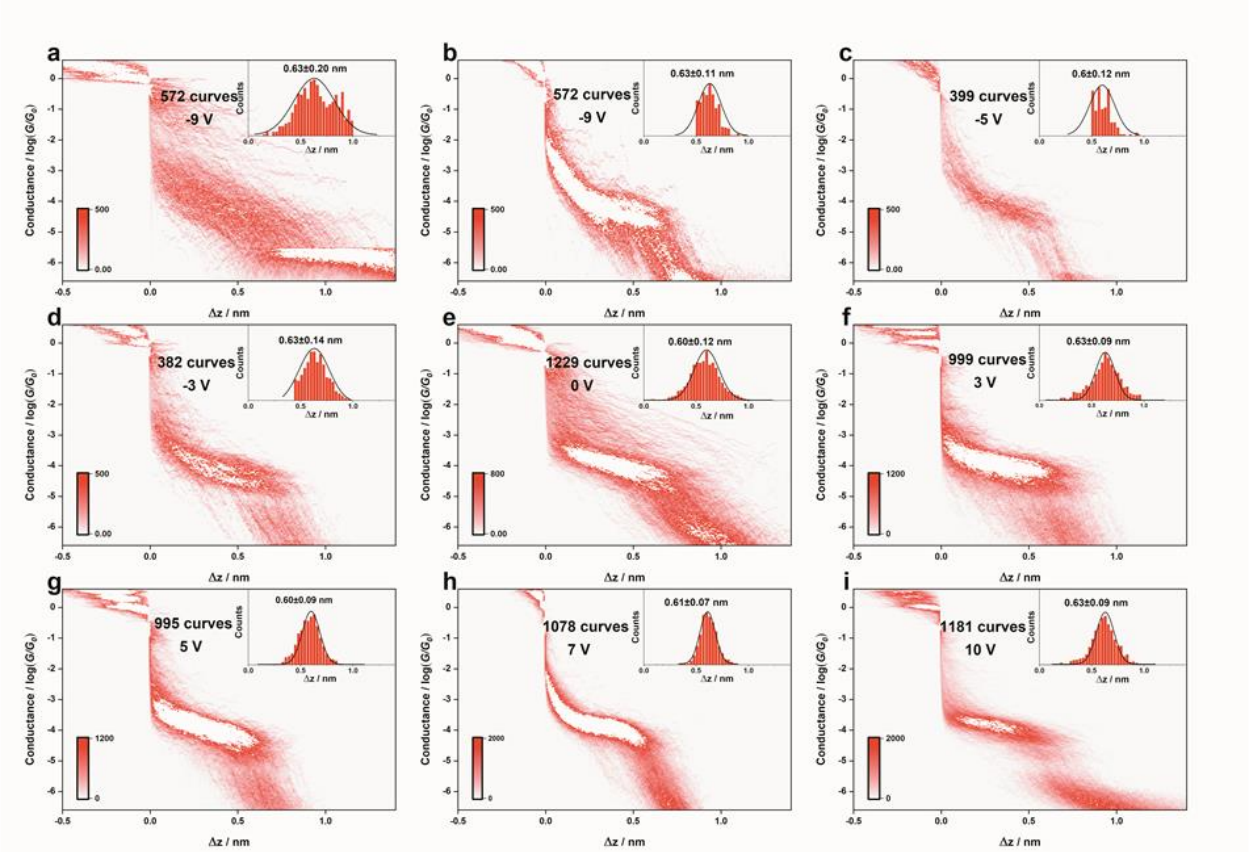

Figure S9. The results of 2D conductance-displacement histograms for **M2** at different V_g. (a) -9 V; (b) -7 V; (c) -5 V; (d) -3 V; (e) 0 V; (f) 3 V; (g) 5 V; (h) 7 V; (i) 10 V.

1D histograms for M3 at different V_g

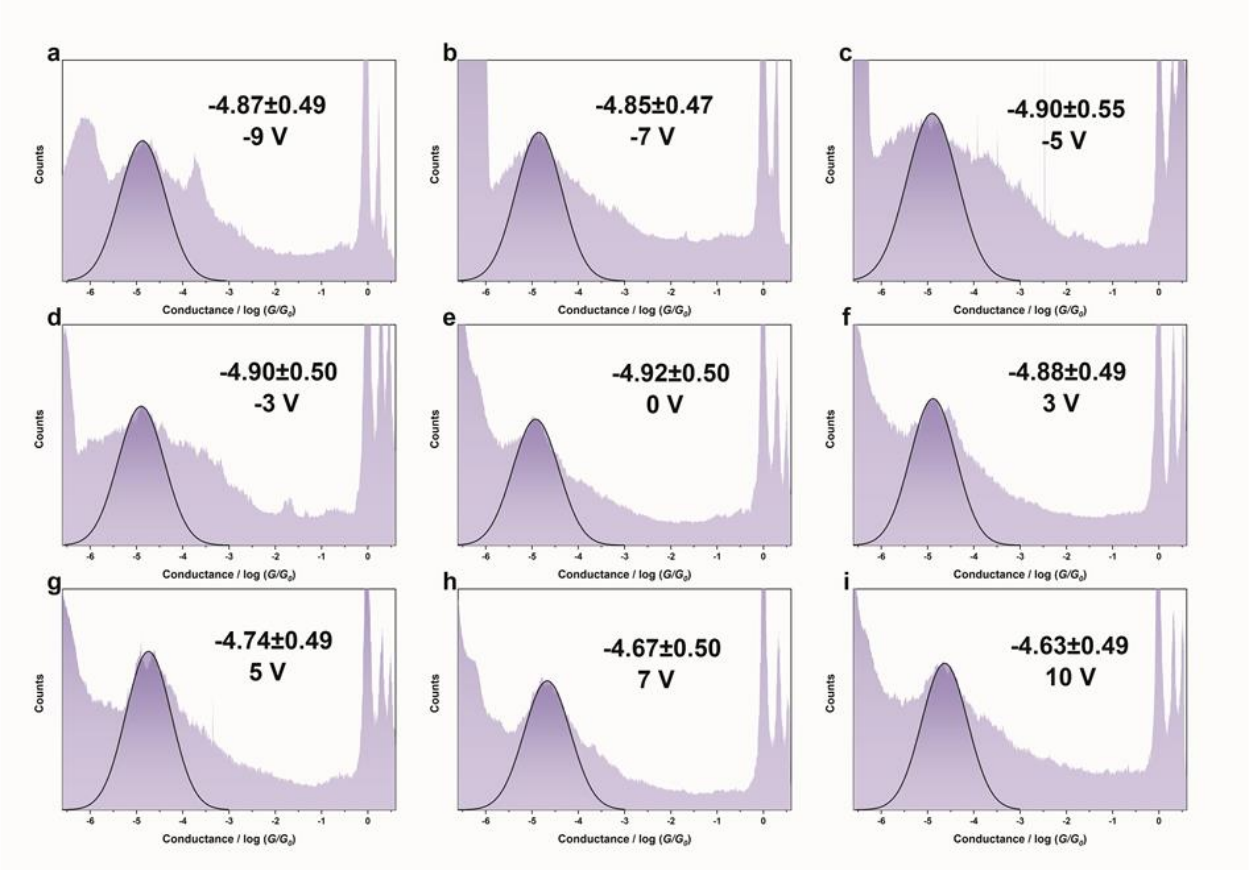

Figure S10. The results of 1D histograms for **M3** at different V_g. (a) -9 V; (b) -7 V; (c) -5 V; (d) -3 V; (e) 0 V; (f) 3 V; (g) 5 V; (h) 7 V; (i) 10 V.

2D conductance-displacement histograms for M3 at different V_g

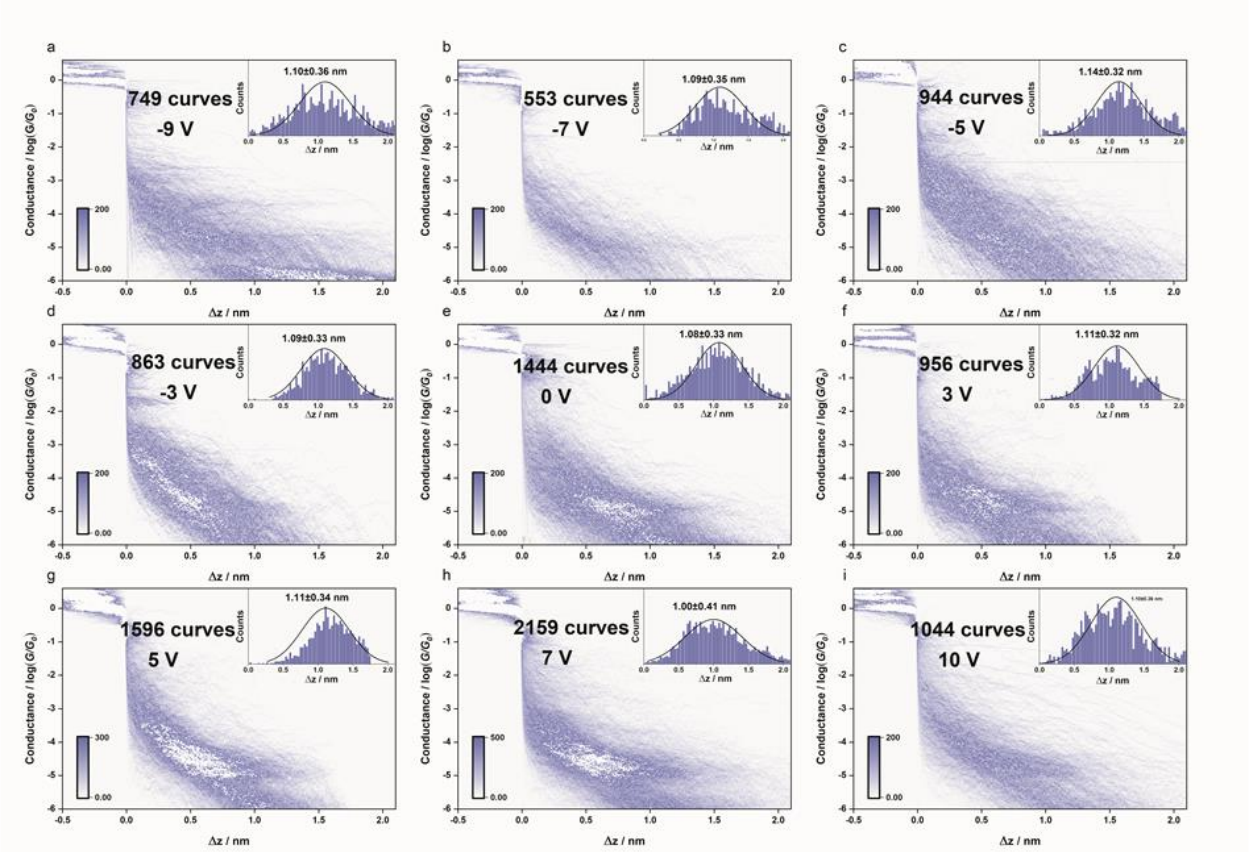

Figure S11. The results of 2D conductance-displacement histograms for **M3** at different V_g. (a) -9 V; (b) -7 V; (c) -5 V; (d) -3 V; (e) 0 V; (f) 3 V; (g) 5 V; (h) 7 V; (i) 10 V.

Table 1. Single-molecule conductance summary

V_g	Conductance / log (G/G_0)		
	M1	**M2**	**M3**
	a ± b		
-9 V	-3.31 ± 0.35	-4.43 ± 0.50	-4.87 ± 0.49
-7 V	-3.37 ± 0.33	-4.31 ± 0.50	-4.85 ± 0.47
-5 V	-3.50 ± 0.31	-4.21 ± 0.48	-4.90 ± 0.55
-3 V	-3.56 ± 0.34	-4.17 ± 0.50	-4.92 ± 0.50
0 V	-3.60 ± 0.35	-4.00 ± 0.45	-4.92 ± 0.43
3 V	-3.67 ± 0.33	-3.98 ± 0.40	-4.88 ± 0.49
5 V	-3.70 ± 0.36	-3.90 ± 0.40	-4.74 ± 0.49
7 V	-3.74 ± 0.35	-3.87 ± 0.30	-4.67 ± 0.50
10 V	-3.80 ± 0.30	-3.83 ± 0.30	-4.63 ± 0.49

The value of a represents the peak value of the one-dimensional graph and the b represents the FWHM/2 using Gaussian fitting.

The conductance changes for another HOMO-dominated system: 5,7-azulene derivative (5,7-Az)

We have performed the conductance measurement of another HOMO-dominated system to confirm the universality. It follows the same trend with **M1**, and the conductance decreases with the increased V_g. We combined with the theoretical calculation, and it proved that the HOMO dominates the charge transport in this system, as shown in Figure S12.

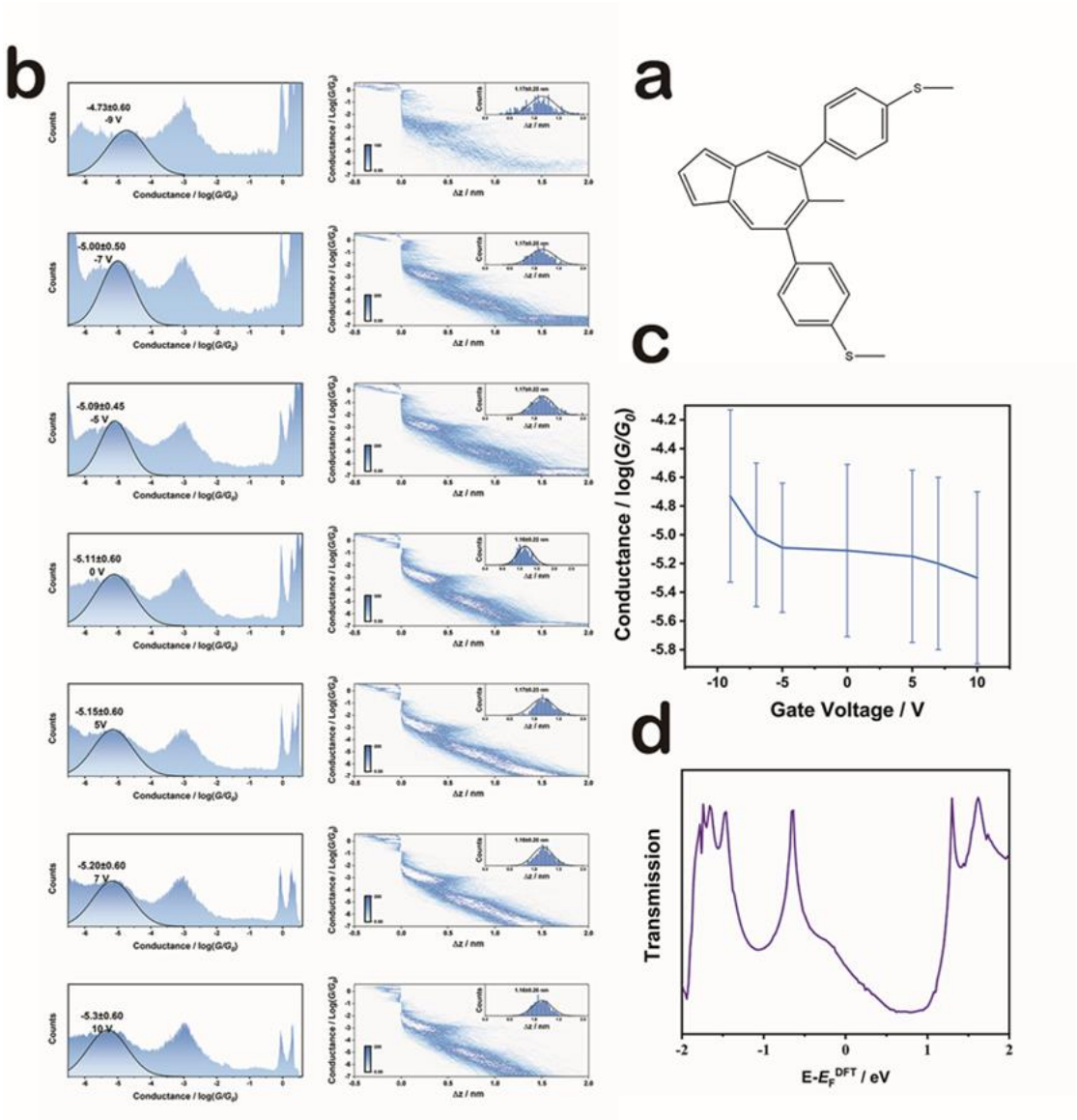

Figure S12. (a) The added molecular structure of **5,7-AZ**. (b) The 1D histograms of conductance variation and 2D histograms under different V_g. (c) The trends of conductance changes for **5,7-AZ**. (d) The calculation transmission spectra for **5,7-AZ**.

S4. The I-V measurement for M1 under different V_g

We have done the I-V measurements to determine the transition voltage when the molecules were hovered in the electrode gap, which helps us qualitatively determine the shifting degree of energy level. The I-V measurements of **M1** molecular junction were recorded by sweeping the source/drain bias voltage between -1 V and 1 V under different gate voltages, thus obtaining the forward/reversed I-V intensity graph and the corresponding fitting curves, as shown in Figure S13 (ab, de, gh). Moreover, we combined all the forward and reversed I-V data to get a comprehensive I-V intensity chart and a final fitting curve, as shown in Figure S13 (c, f, i).

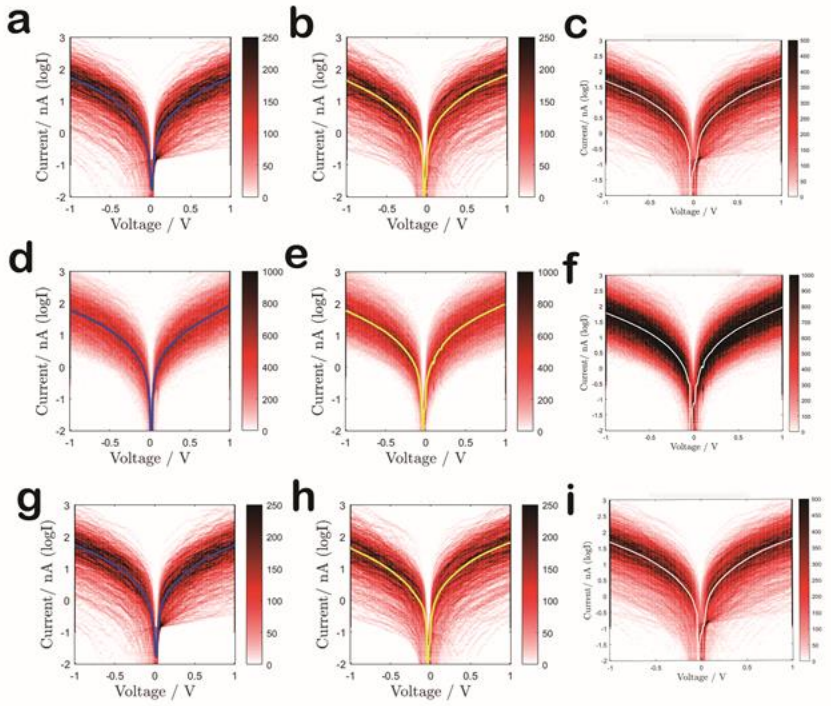

Figure S13. The I-V result for **M1** under the different gate voltage. (a-c) V_g = -5 V; (d-f) V_g = 0 V; (g-i) V_g = -5 V. (The blue line represents the I-V curve fitted by the forward sweep, the yellow line represents the I-V curve fitted by the reversed sweep, the white line was the combination of the forward and reversed swept curves).

The transition voltage spectroscopy (TVS) of **M1** was obtained by transforming the I-V into Fowler-Nordheim plot ($\ln(I/V^2) \sim 1/V$), as shown in Figure S14. The transition voltage can be obtained by reading the minimum point.[7] The result of TVS measurements agrees with our trends of conductance gating. For **M1**, when the V_g changes from negative to positive, the conductance decreases, which indicate the increase of the energy gap between electrode Fermi level and frontier molecule orbital increase, therefore, the transition voltage will increase, as expected from the TVS measurement, which rises from 0.45 eV at -5 V_g to 0.68 eV at +5 V_g.

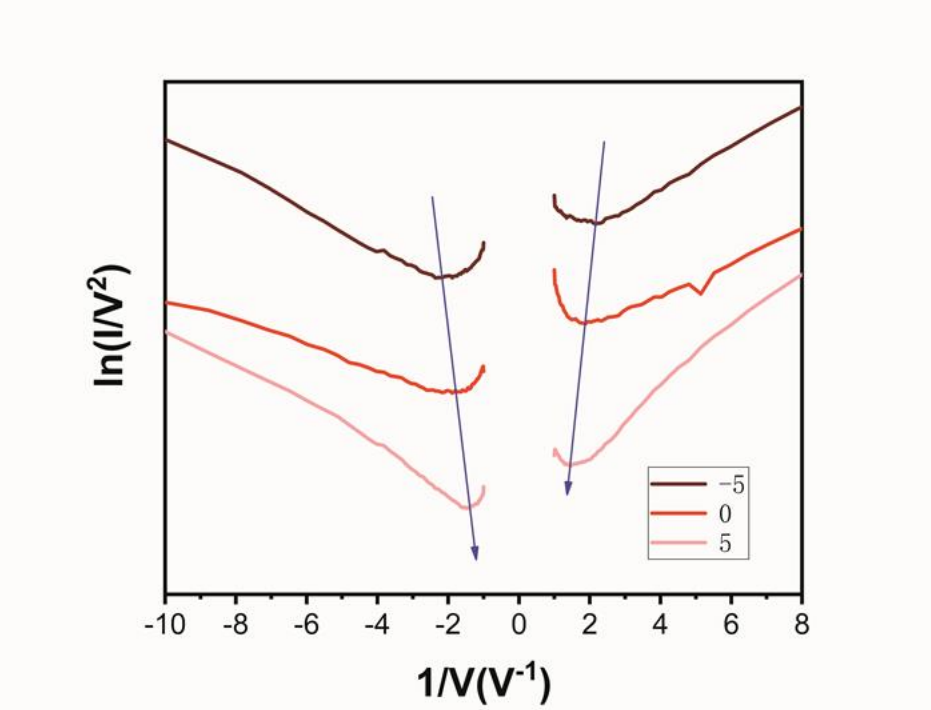

Figure S14. The transition voltage spectroscopy under different V_g for **M1**.

S5. Other control experiments

The control experimental to exclude the thermal effects.

We carried out the control experiment under variable temperatures through heating the substrate to confirm that the conductance change is due to the V_g for **M1** through our home-built single-molecule thermoelectricity measuring system.[8] We first record the conductance at room temperature. We increased the temperature at every step of 5 K, the results, as shown in Figure S15. We found that it is not affected by the temperature.

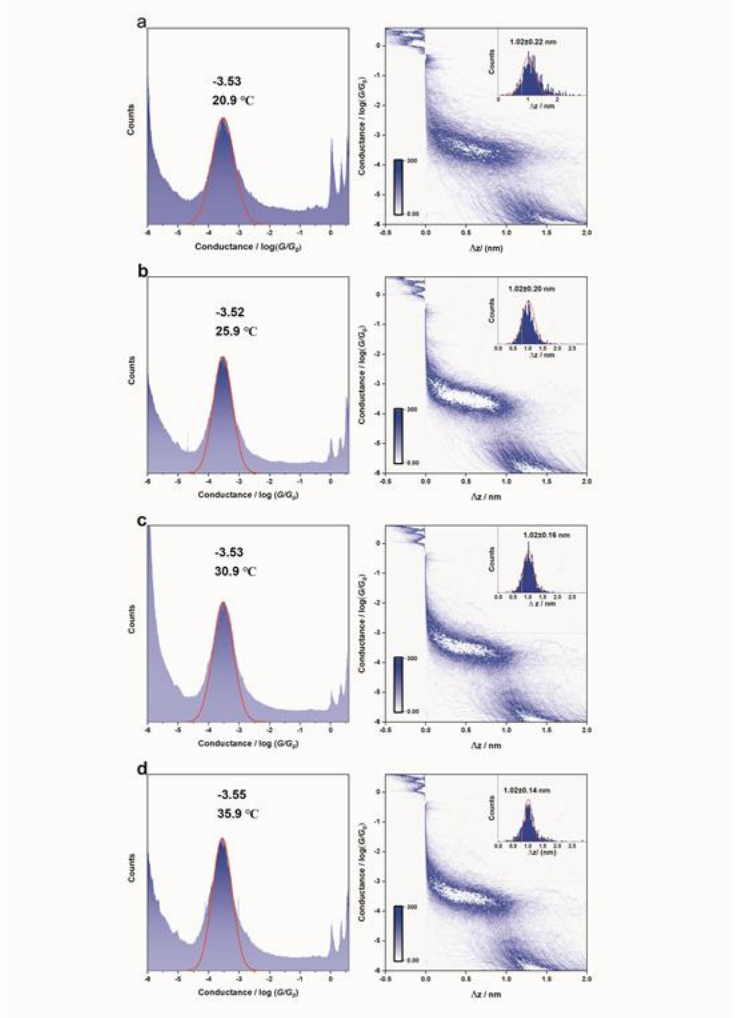

Figure S15. The conductance variation under different temperatures for **M1**.
(a) 20.7 ℃; (b) 25.7 ℃; (c) 30.7 ℃; (d) 35.7 ℃.

The control experimental to comment the contributions of phenyl rings rotation

Many articles reported the electric field could facilitate the planarization by rotating the phenyl rings.[1, 9, 10] Therefore, we performed the control experiment under different source/drain biases at the V_g = 0 for **M1**, the result shows that conductance changes are small due to the phenyl rings' torsion effect, which further confirmed that the conductance variation are mainly due to the gate modulation.

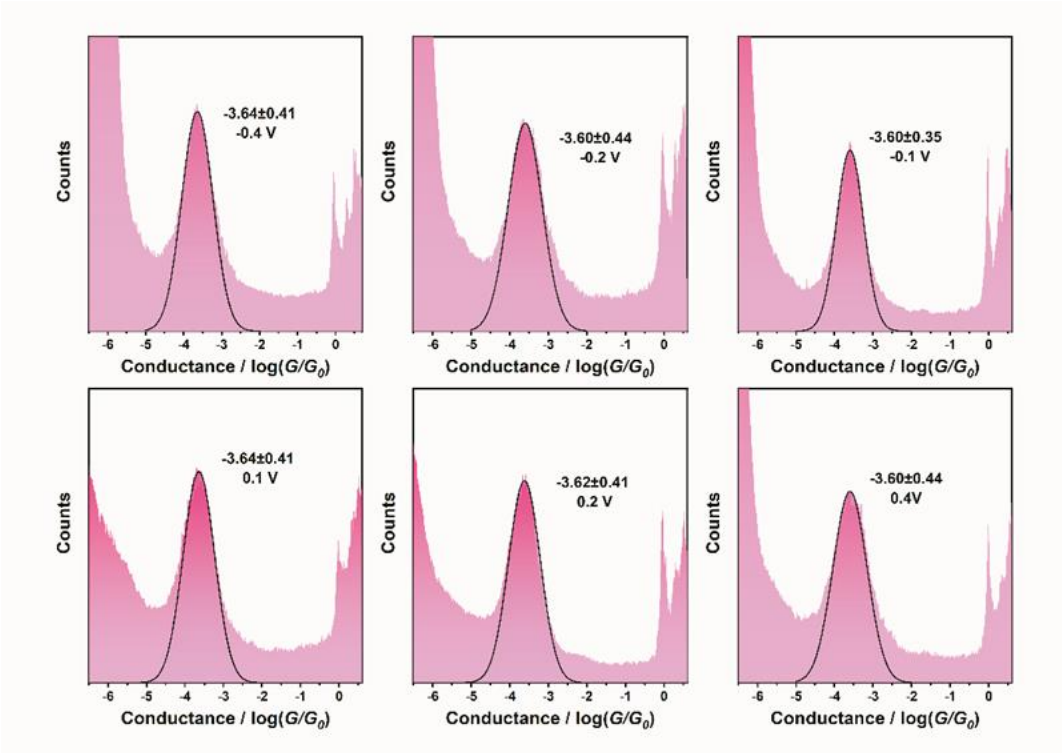

Figure S16. The 1D histograms of conductance variation under different source/drain biases for **M1**.

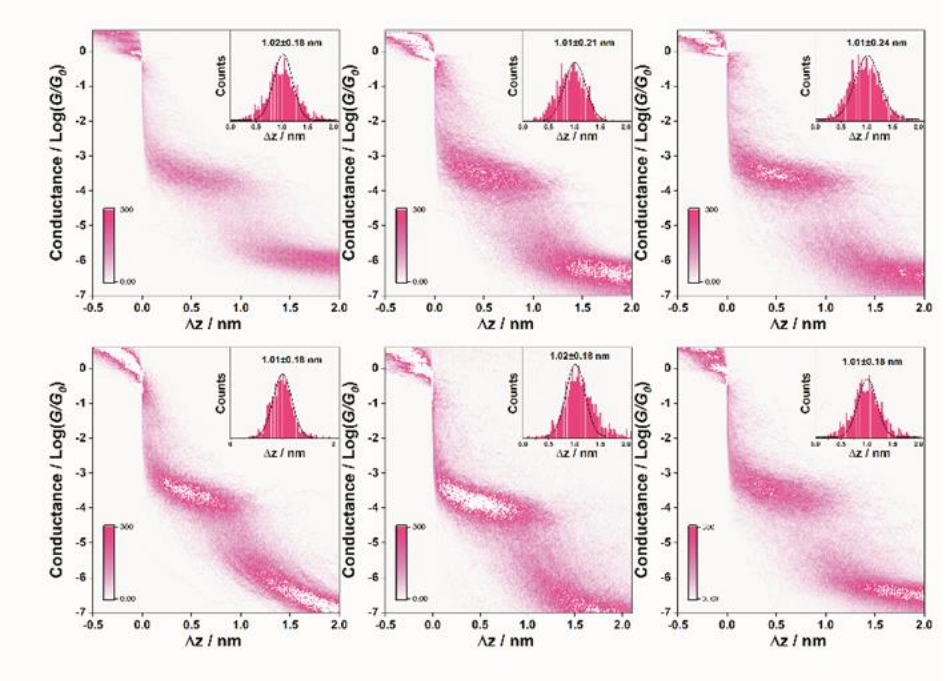

Figure S17. The 2D histograms under different source/drain biases for **M1**.

S6. Theoretical calculations

Simulated the gate coupling using COMSOL Multiphysics for M1

We have simulated the gate-coupling degree using COMSOL Multiphysics.[11] Considering the actual situation is difficult to be modeled (such as the huge scale differences between molecules and chips, the high-speed molecular motion and so on), we have made some reasonable simplifications of the model by reducing the model size while keeping the proportion of the HfO_2 layer to the gate electrode remains unchanged and considering the irregularly shaped molecule as a cylinder, and the conductance of the cylinder is the experimental conductance of **M1**. The final model is shown in Figure S18.

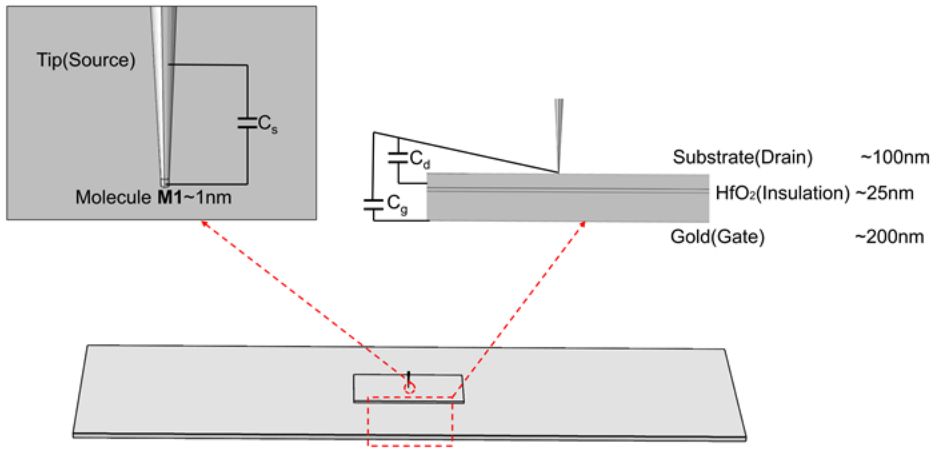

Figure S18. The model and detailed information of back-gated molecular junction of **M1** in COMSOL Multiphysics.

The capacitance between the molecule and the gate electrode (C_g) can be calculated using $C_g=Q/V_g$.[12] Besides, all parts of the system can be regarded as the conductors so that we can think of the model as a multi-conductor system. In this case, we need to consider the C_g, C_s, $C_{d,}$ which means

the partial capacitance between the molecule and the gate electrode, the molecule and the source electrode, the molecule and the drain electrode, respectively, when the molecule of **M1** is applied in the unit gate voltage. Based on these prerequisites, we successfully built the model with the built-in function of COMSOL to calculate the spatial charge density of source, gate and drain electrodes and get the corresponding charge by volume integration. The spatial charge density distribution is shown in Figure S19. Another critical parameter for the gate-coupling system is γ, which means the averaged molecular potential V_m in response to a change in V_g, and the simulated γ (γ_1) is 0.038 by calculation from the above model as shown in Table 2 of ESI and below,[13] which accorded with the experimental γ (γ_2, 0.035), calculated according to the simulated transmission spectra (the energy was theoretically shifted around 0.32 eV when the conductance varies from $10^{-3.32}$ G_0 to $10^{-3.62}$ G_0 under the V_g range from -9 V to 0 V. Hence, the average value of the molecular potential in response to the change in V_g is 0.035)

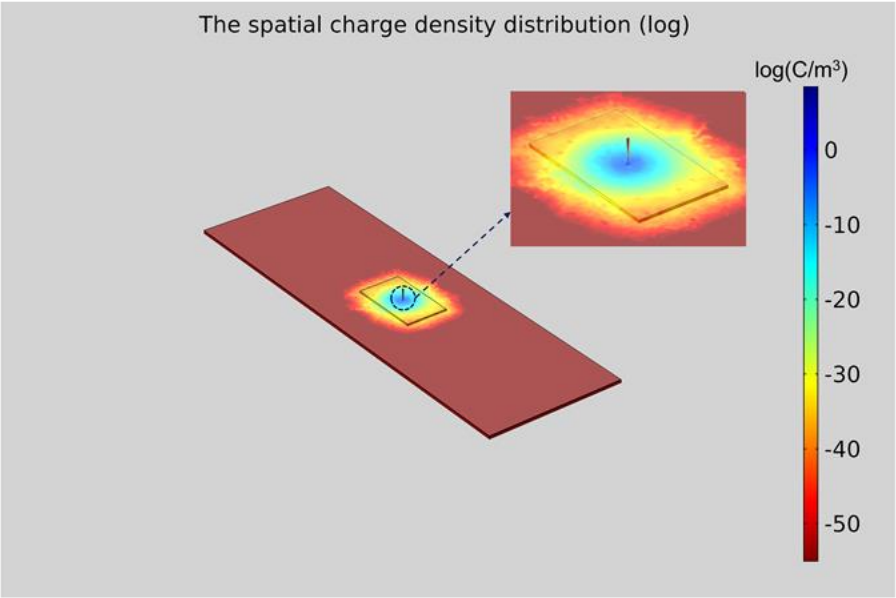

Figure S19. The spatial charge density distribution for **M1** under V_g = -1 V (C/m^3, in logarithmic scale)

Table 2. Simulated effective capacitance and coupling coefficient

C_d (F)	C_s (F)	C_g (F)	γ_1 ($\gamma \sim C_g / C_d + C_s + C_g$)	γ_2
7.09E-21	5.45E-21	4.95E-22	0.038	0.035

We analyzed the differences between γ_1 and γ_2. First, the quantum effects haven't been taken into consideration in the simulation model, however, there are some literatures about the calculation of capacitance between nano-objects which shows that quantum effects have minimal impact on the effective capacitance.[14] Second, the experimental materials' electrical properties are a definite range, we can only estimate one value from it. Third, the morphology and size of the source, gate, drain electrodes and insulating layer also influence the final simulation results.[13, 15] In spite of those, we consider our simulations and estimations about gating efficiency are reasonable.

Theoretical calculations of the transmission spectra

The configuration optimization of **M1**-**M3** was carried out by Gaussian 16,[16] the optimization molecules, as shown in Figure S20 (a), the angle between the three benzene rings is 37 degrees. The SIESTA is then used to optimize the device configurations found on density functional theory (DFT).[17] We use the Generalized Gradient Approximation-Perdew Burke Ernzerh (GGA-PBE) exchange-correlation functional and double-ζ polarized (DZP) basis set is adopted for all atoms except the Au atoms to obtain a breakneck computing speed.[18] We choose the max force tolerance as 0.05 eV/ Å, and the mesh cut off is 150.0 Ry at 300 K. The optimized device configuration is shown in Figure S20 (b). Finally, we calculated the zero-bias transmission spectrum combined with the Gollum quantum transport code in the Atomistix Tool Kit (ATK) package software. The three molecules' transmission spectra are shown in Figure S20 (c).

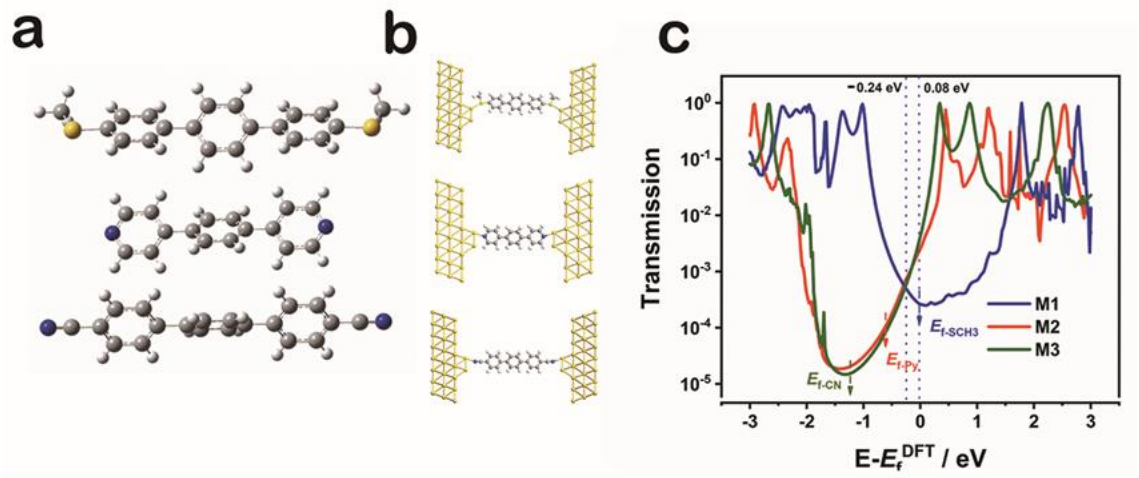

Figure S20. (a) The optimized molecule configurations using Gaussian 16. (b) The optimized device configurations. (c) The transmission spectra for **M1**-**M3** (The arrow represents the Fermi level position, dotted lines represent the energy positions under different conductance.

Because –Py (**M2**) and –CN (**M3**) anchors are strong electron-withdrawing groups, which significantly affect the Fermi level's position. Furthermore, if we use the conventional density functional theory (DFT) to calculate the transmission spectra, which will make the Fermi level are very close to the lowest unoccupied molecular orbital (LUMO). Other articles reported that self-energy-corrected density functional theory (DFT) and a coherent scattering-state approach could be used for the transmission spectra calculation of such systems.[19] However, the standard method can be used for determining the type of transport in our study systems, thus we did not use the above-complicated method. Besides, we compared the transmission spectra of similar systems in other literatures, the transmission spectra we calculated is very similar to theirs.[20] Moreover, the $–SCH_3$ anchor does not require energy correction to obtain the energy level of the frontier molecular orbital and the Fermi level accurately. To ensure the accuracy of the calculation, we also made a comparison and found it is consistent with the calculation results of relevant literature.[1] Besides, we considered the location of the Fermi level in the transmission according to the experimental conductance,[8] as shown in Figure S20.

We can see a different electrode configuration for **M2** compared with **M1** and **M3**, because we use the electrode model of **M1** and **M3** to calculate **M2**, the transmission spectra will arise with some other impurity peaks, and the transmission spectra will no longer be smooth, which will be inconsistent with the other articles reported. Therefore, we adjust the same electrode configuration to calculate the transmission spectra of **M2** as below. We find that the electrode configurations have a minimal effect on the transmission functions of **M2** in our works, as shown in Figure S21.

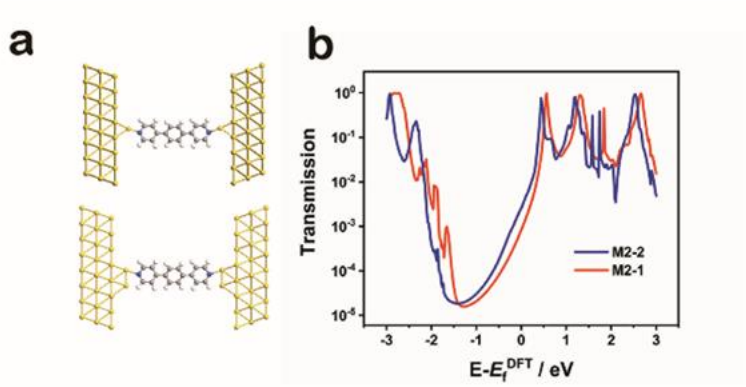

Figure S21. (a) The different configurations for **M2** (b) the transmission spectra of **M2** with different electrode configurations.

S7. The influence of the dielectric layer's thick on the gating efficiency

To improve the gating efficiency, we tried to reduce the thickness of the insulating layer. We prepared the chips with a dielectric layer of 15 nm for comparison. There is a similar but slightly larger conductance variation trend than those obtained from the chips of 25 nm for M1. The corresponding results are shown as below.

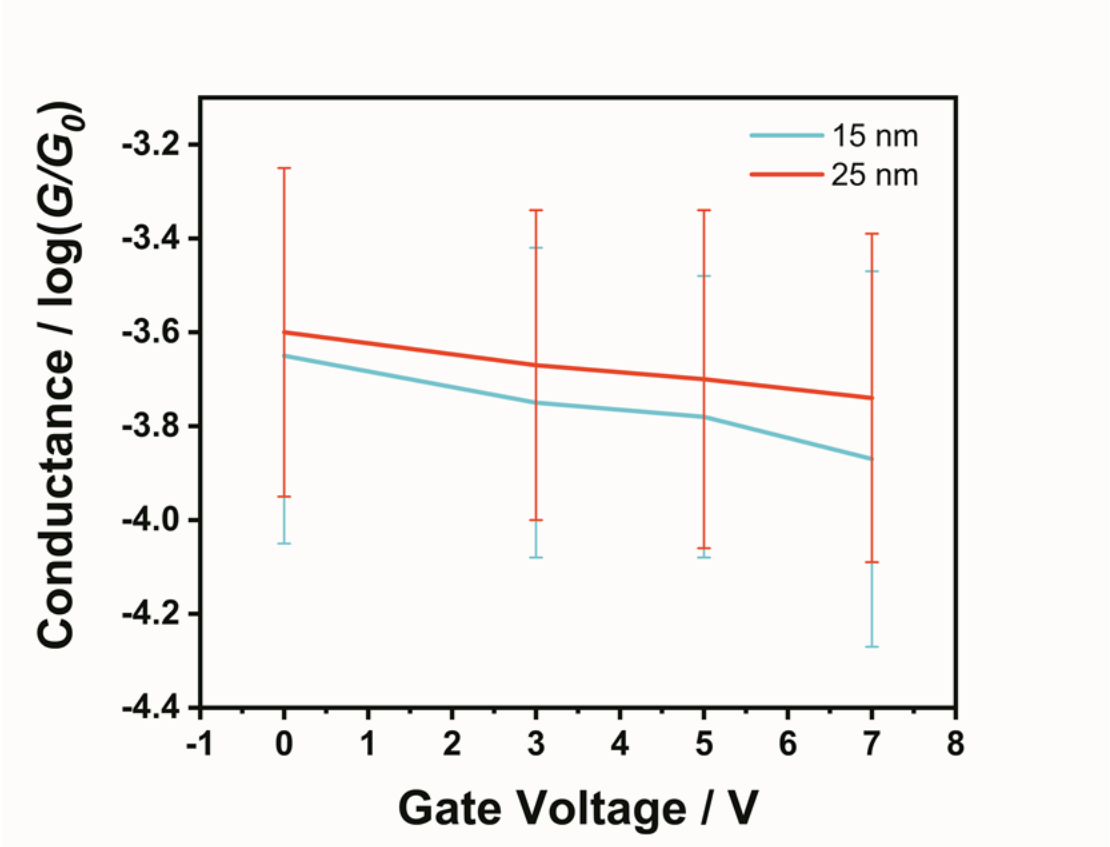

Figure S22. The variation trend of conductance with V_g with different thicknesses of the dielectric layer for **M1** (the red line represents 25 nm, and the blue line represents 15 nm, the error bar represents the FWHM/2 of conductance peak using Gaussian fitting).

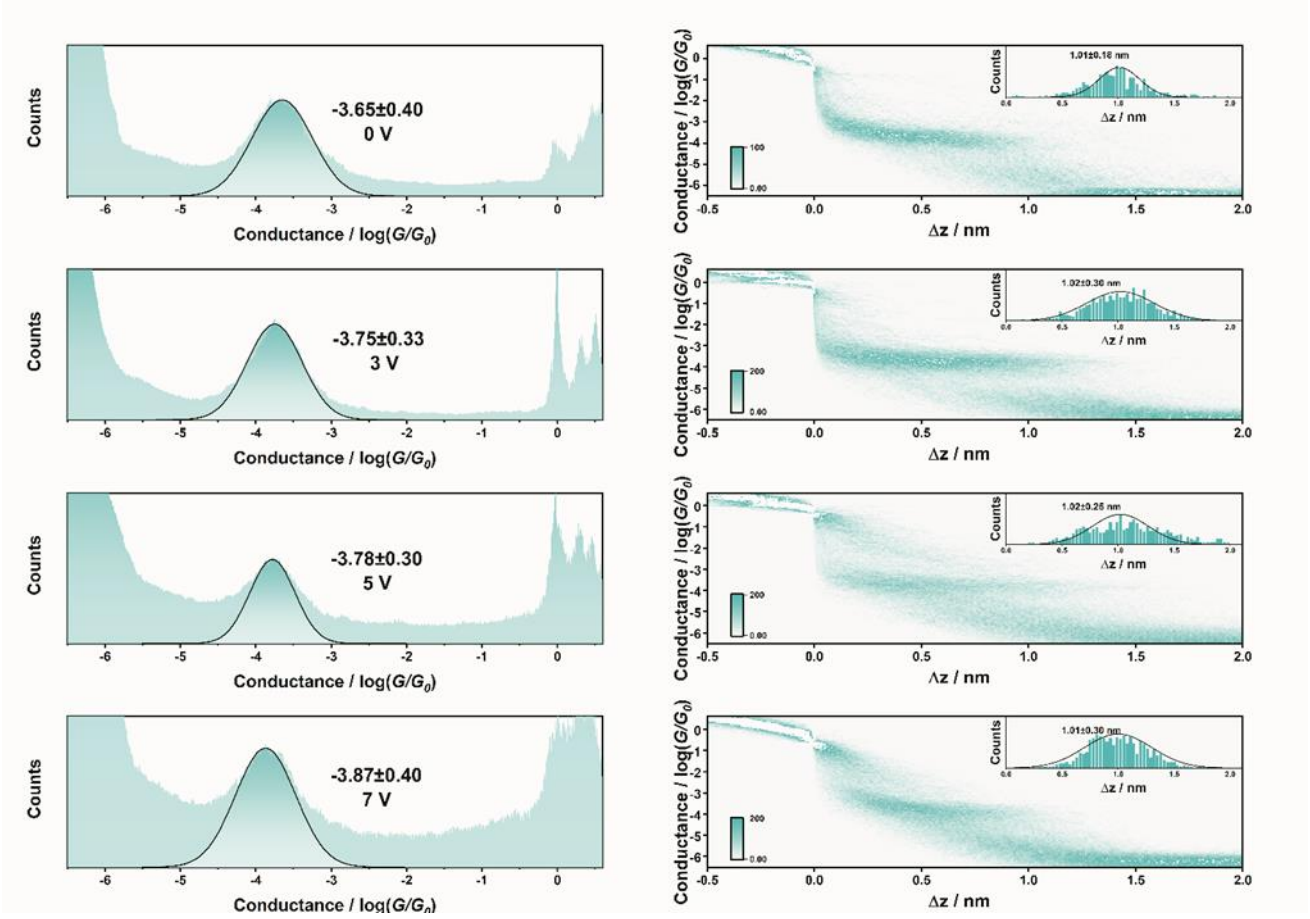

Figure S23. The 1D histograms of conductance and the 2D histograms under different V_g for **M1** using substrates with 15 nm insulating layer.

References

1. Y. Tang, Y. Zhou, D. Zhou, Y. Chen, Z. Xiao, J. Shi, J. Liu and W. Hong, *J. Am. Chem. Soc.*, 2020, **142**, 19101-19109.
2. H. Yuan, D. C. Riley, Z.-X. Shen, P. A. Pianetta, N. A. Melosh and R. T. Howe, *Nano Energy*, 2017, **32**, 67-72.
3. D. Blaschke, F. Munnik, J. Grenzer, L. Rebohle, H. Schmidt, P. Zahn and S. Gemming, *Appl. Surf. Sci.*, 2020, **506**, 144188.
4. F. Jiang, D. I. Trupp, N. Algethami, H. Zheng, W. He, A. Alqorashi, C. Zhu, C. Tang, R. Li, J. Liu, H. Sadeghi, J. Shi, R. Davidson, M. Korb, A. N. Sobolev, M. Naher, S. Sangtarash, P. J. Low, W. Hong and C. J. Lambert, *Angew. Chem. Int. Ed.*, 2019, **58**, 18987-18993.
5. M. Baghernejad, D. Z. Manrique, C. Li, T. Pope, U. Zhumaev, I. Pobelov, P. Moreno-Garcia, V. Kaliginedi, C. Huang, W. Hong, C. Lambert and T. Wandlowski, *Chem. Commun.*, 2014, **50**, 15975-15978.
6. K. Moth-Poulsen, L. Patrone, N. Stuhr-Hansen, J. B. Christensen, J. P. Bourgoin and T. Bjornholm, *Nano Lett.*, 2005, **5**, 783-785.
7. H. Song, Y. Kim, Y. H. Jang, H. Jeong, M. A. Reed and T. Lee, *Nature* 2009, **462**, 1039-1043.
8. H. Chen, S. Sangtarash, G. Li, M. Gantenbein, W. Cao, A. Alqorashi, J. Liu, C. Zhang, Y. Zhang, L. Chen, Y. Chen, G. Olsen, H. Sadeghi, M. R. Bryce, C. J. Lambert and W. Hong, *Nanoscale*, 2020, **12**, 15150-15156.
9. D. Kos, G. Di Martino, A. Boehmke, B. de Nijs, D. Berta, T. Földes, S. Sangtarash, E. Rosta, H. Sadeghi and J. J.

Baumberg, *Nat. Commun.*, 2020, **11**, 5905.
10. K. M. Blacklock, B. J. Yachnin, G. A. Woolley and S. D. Khare, *J. Am. Chem. Soc.*, 2018, **140**, 14-17.
11. W. W. Kilarski, C. Martin, M. Pisano, O. Bain, S. A. Babayan and M. A. Swartz, *Nat. Commun.*, 2019, **10**, 2895.
12. D. R. Khanal and J. Wu, *Nano Lett.*, 2007, **7**, 2778-2783.
13. A. W. Ghosh, T. Rakshit and S. Datta, *Nano Lett.*, 2004, **4**, 565-568.
14. Y. S. Gerasimov, V. V. Shorokhov, A. G. Maresov, E. S. Soldatov and O. V. Snigirev, *Journal of Communications Technology and Electronics*, 2011, **56**, 1483-1489.
15. V. Kolkovsky, K. Lukat, E. Kurth and C. Kunath, *Solid-State Electron.*, 2015, **106**, 63-67.
16. M. Frisch, G. Trucks, H. Schlegel, G. Scuseria, M. Robb, J. Cheeseman, G. Scalmani, V. Barone, G. Petersson and H. Nakatsuji, *In Revision A, Gaussian, Inc., Wallingford CT*, 2016.
17. J. M. Soler, E. Artacho, J. D. Gale, A. Garc á, J. Junquera, P. Ordej ón and D. S ánchez-Portal, *J. Phys-Condens. Mat.*, 2002, **14**, 2745-2779.
18. J. P. Perdew, K. Burke and M. Ernzerhof, *Phys. Rev. Lett.*, 1996, **77**, 3865-3868.
19. P. Darancet, J. R. Widawsky, H. J. Choi, L. Venkataraman and J. B. Neaton, *Nano Lett.*, 2012, **12**, 6250-6254.
20. W. Hong, D. Z. Manrique, P. Moreno-Garc á, M. Gulcur, A. Mishchenko, C. J. Lambert, M. R. Bryce and T. Wandlowski, *J. Am. Chem. Soc.*, 2012, **134**, 2292-2304.